JOURNAL OF OPTOELECTRONICS AND ADVANCED MATERIALS Vol. 9, No. 9, September 2007, p. 2813 - 2819

Step-by-step parameter-extraction method for high-speed vertical cavity laser's rate-equation model

V. V. LYSAK[a,b], K. S. CHANG[a], Y. M. SONG[a], YONG TAK LEE[a*]
[a]*Department of information and communication, Gwangju Institute of science and technology (GIST), 1 Oryong-dong, Buk-ku, Gwangju, 500-712, Republic of Korea*
[b]*Laboratory "Photonics", Kharkov National University of Radio Electronics, 14, Lenin av., Kharkov, 61166, Ukraine*

Values for parameters in a rate equation description of a vertical-cavity surface emitting laser (VCSEL) must be appropriately selected in order to obtain agreement between the calculated and measured results regarding system performance. Here, a technique is described for readily extracting values of the rate equation parameters using measurements of light-current and small-signal modulation characteristics for a bias current well above the threshold current. The calculated and measured data for the device are in good agreement.

(Received August 6, 2007; accepted August 23, 2007)

Keywords: Multiple-quantum-wells, Parameter extraction, Rate equation model, Small-signal modulation characteristics, VCSEL

1. Introduction

VERTICAL-CAVITY SURFACE-EMITTING LASERS (VCSELs) are becoming desirable candidates for many short-distance fiber-optic applications and free-space parallel optical interconnects because of their low-threshold, high-efficiency, high-speed operation, low divergent output beam, and the possibility to manufacture on-wafer testable, large, 2D VCSEL arrays.

One of the ongoing current activity standards for 10Gb Ethernet, the issue of most convenient and economical source for such data-communications is now being deliberated. Vertical-cavity surface-emitting lasers (VCSEL's) having higher bandwidths greater than 10 GHz, which are expected to play a key role for these next-generation network transceivers [1].

As the bit rates of high-speed transmission systems increase, the dynamic properties of laser diodes like the resonance frequency and damping factor are becoming increasingly important [2].

Most VCSELs contain a multiple-quantum-well (MQW) structure with a complicated dynamic response, and design parameters such as nonlinear gain effects [3], [4], carrier leakage [5], and capture-escape processes in QW [6]. These parameters can have a profound effect on both the resonance frequency and damping behavior. In order to understand this behavior, it is necessary to fully characterize CW and the small-signal modulation behavior of a large number of different MQW designs, which requires the use of simple laser structures and a robust measurement technique.

In [7,8] we simulated the VCSEL including the thermal effects

To estimate the system performance, a rate equation description of the laser is often used. In this estimation, as the complexity of the model increases more detailed knowledge of the laser is required, and the computational time required for the system performance calculations subsequently increases. However, while sophisticated models can provide considerable insight into important characteristics of lasers for system simulations, a relatively simple model is often adequate [6,9]. The parasitic elements and rate-equation model parameters can be obtained from light-current and modulation response measurements by using numerical optimization techniques [10–13].

Nonetheless, in order to obtain agreement between experimental and calculated results, values for the parameters appearing in the rate equations must be appropriately selected. In this paper, the model consists of the maximum number of parameters that can be analytically described. It is shown that a large number of parameters can be considered, as small variations of parameter values can reproduce the measured results.

2. VCSEL rate equation model

The modulation dynamics of VCSEL with MQW active layer are easily modeled by coupled rate equations, which describe the carrier number in the SCH layer (N_B) and the quantum well (N_W); the photon number in the mode cavity (N_P), are written as

$$\frac{\mathrm{d}N_B}{\mathrm{d}t} = \frac{\eta_i I}{q(1+E_I I)} - \frac{N_B}{\tau_s} + \frac{N_W}{\tau_e}, \qquad (1)$$

$$\frac{\mathrm{d}N_W}{\mathrm{d}t} = \frac{N_B}{\tau_s} - \frac{N_W}{\tau_e} - \frac{N_W}{\tau_{eff}} - \frac{G_d\left(N_W - N_{W,T}\right)N_P}{\left(1+E_P N_P\right)\left(1+E_e N_W\right)}, \qquad (2)$$

$$\frac{\mathrm{d}N_P}{\mathrm{d}t} = N_P\left[\frac{G_d\left(N_W - N_{W,T}\right)}{\left(1+E_P N_P\right)\left(1+E_e N_W\right)} - \frac{1}{\tau_P}\right] \tag{3}$$

where q is the electron charge; η_i is the fraction of terminal current that provides carriers in the SCH region; $E_I = 1/I_{leak}$ is the parameter for description of leakage current through the whole structure due to diode-like drift [5]; $N_B = n_{sch}V_{sch}$ and $N_W = n_w V_w$ are the number of carriers in the SCH and QW, respectively, n_{sch} and n_w are the carrier concentrations in the SCH and QW; $V_{sch} = 2\pi R^2 t_{sch}$ and $V_w = N_{qw}\pi R^2 t_w$ are the volumes of the SCH and QW layers; R is the active layer radius; t_{sch} and t_w are thickness of the SCH and QW layers; N_{qw} is the number of QWs; $N_P = \Gamma n_p V_w$ is the number of photons in the mode cavity; Γ is the optical confinement factor; $G_d = \Gamma v_g V_{qw}\partial g/\partial n_w$ is the normalized differential gain coefficient; v_g is the group velocity; $\partial g/\partial n_w$ is the differential gain; $N_{W,T}$ is the carrier numbers at the transparency; E_P and E_e are nonlinear coefficients due to influence of photons and carriers on the optical gain; τ_s, τ_e, and τ_{eff} are the ambipolar transport, escape, and carrier life times [6]; and $\tau_P = 1/\left(v_g\left(\alpha_i+\alpha_m\right)\right)$ is the photon life time [14], α_m and α_i are incremental internal modal power and distributed mirror loss< respectively; $v_g = c/n_g$ is the group velocity, c is the speed of light, n_g is the group refractive index.

The output optical power is given by

$$N_{P0}\left(P_0\right) = \frac{\tau_P}{\eta_0 E_g}P_0 \tag{4}$$

where $\eta_0 = \alpha_m/\left(\alpha_i+\alpha_m\right)$ is the differential quantum efficiency; $E_g = hc/\lambda$ is the energy band-gap, h is Planck's constant, and λ is the optical wavelength.

At the steady state condition $dN_B/dt = 0$, $dN_W/dt = 0$, $dN_P/dt = 0$, the number of carriers in QW and the total current can be presented as a function of photons as:

$$N_{W0}\left(N_{P0}\right) = \frac{1+E_P N_{P0}+\tau_P G_d N_{W,T}}{G_d\tau_P - E_e\left(1+E_P N_{P0}\right)} \tag{5}$$

and

$$I_0\left(N_{P0}\right) = \frac{qI_s}{\eta_i - qI_s E_I}, \tag{6}$$

$$I_S = \frac{1+E_P N_{P0}+\tau_P G_d N_{W,T}}{\tau_{eff}\left(G_d\tau_P - E_e\left(1+E_P N_{P0}\right)\right)} + \frac{N_{P0}}{\tau_P}.$$

A small-signal solution of the equations is done by first making the following substitutions: $I = I_0 + \Delta I\exp\left(j\omega t\right)$;

$$N_B = N_{B0} + \Delta N_{B0}\exp\left(j\omega t\right);$$
$$N_W = N_{W0} + \Delta N_{W0}\exp\left(j\omega t\right); \text{ and}$$
$$N_P = N_{P0} + \Delta N_{P0}\exp\left(j\omega t\right);$$

Then the optical gain change can be presented as a sum of partial changes of carriers and photons as

$$\Delta\left(G\left(N_W,N_P\right)N_P\right) = G\left(N_{W0},N_{P0}\right)\Delta N_P + N_{P0}\left(\frac{\partial G}{\partial N_W}\Delta N_W + \frac{\partial G}{\partial N_P}\Delta N_P\right). \tag{7}$$

$$\frac{\partial G}{\partial N_W} = \frac{G_d\left(1+E_e N_{W,T}\right)}{\left(1+E_P N_{P0}\right)\left(1+E_e N_{W0}\right)^2}; \tag{8}$$

$$\frac{\partial G}{\partial N_P} = -\frac{E_p}{\tau_p\left(1+E_P N_{P0}\right)}. \tag{9}$$

After the small-signal quantities are substituted into (1)-(3) and the steady-state terms are set to zero, the set of small-signal equations can be reduced to a relationship between the modulating current and the number of photons $H\left(\omega\right) = \Delta N_P\left(\omega\right)/\Delta I$ and the relative modulation response can be presented as:

$$R\left(\omega\right) = \frac{H\left(\omega\right)}{H\left(0\right)} = \left(1+j\omega\tau_s\right)\frac{\omega_r^2}{\omega_r^2 - \omega^2 + j\omega\gamma_r} \tag{10}$$

Here γ_r is the damping factor

$$\gamma_r = \frac{1}{\chi\tau_{eff}} + N_{P0}\left(\frac{1}{\chi}\frac{\partial G}{\partial N_W} - \frac{\partial G}{\partial N_P}\right), \tag{11}$$

and ω_r^2 is the square of angular resonance frequency

$$\omega_r^2 = \frac{1}{\tau_p\chi}\frac{\partial G}{\partial N_W}N_{p0} - \frac{1}{\tau_{eff}}\frac{\partial G}{\partial N_p}N_{p0}, \tag{12}$$

where χ is the transport factor:

$$\chi = 1+\tau_s/\tau_e. \tag{13}$$

From (11) and (12) a relationship for K factor can be derived as

$$\gamma_r = K\omega_r^2 + \frac{1}{\chi\tau_{eff}}, \tag{14}$$

where K is Petermann factor:

$$K = \left(\frac{1}{\chi}\frac{\partial G}{\partial N_W} - \frac{\partial G}{\partial N_P}\right)\Bigg/\left(\frac{1}{\tau_p\chi}\frac{\partial G}{\partial N_W} - \frac{1}{\tau_{eff}}\frac{\partial G}{\partial N_p}\right) \tag{15}$$

3. Investigated VCSEL structure

The schematic representation of the investigated 980 nm intracavity-contacted oxide-confined (ICOC) VCSEL

is presented in Fig. 1. As can be seen, the active layer contains three 80 Å $In_{0.2}Ga_{0.8}As$ quantum wells (QWs), separated by 100 Å GaAs barrier between the 150 Å separate confinement heterostructure (SCH) barriers. The resonator contains two $Al_{0.32}Ga_{0.68}As$ spacer layers to form a single wavelength cavity. Then, the cavity is bounded on each side by p- and n-doped $Al_{0.98}Ga_{0.02}As$ oxidation layers, followed by 7/4 λ-thick p- and 5/4 λ-thick n-doped GaAs contact layers. Both sides of the $Al_{0.98}Ga_{0.02}As$ oxidation layers were step graded in order to reduce the resistance. The p–contact layer is divided into two parts with different doping concentration (3λ/4 with a doping concentration of 4×1018 cm^{-3} and 4λ/4 with a doping concentration of 2×1018 cm^{-3}) to suppress the carrier crowding effect [15].

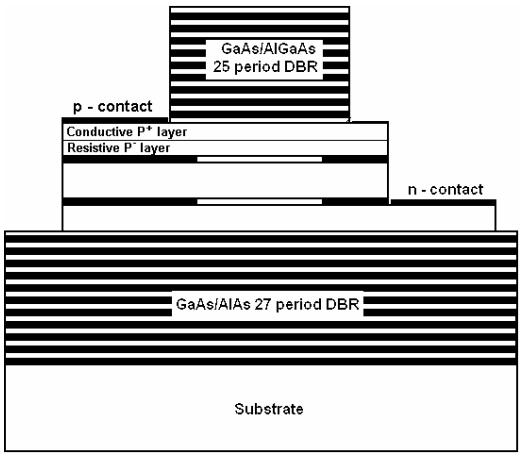

Fig. 1. Schematic presentation of an intracavity - contacted oxide-confined (ICOC) VCSEL structure with asymmetrical contacts.

Oxide windows are formed by the lateral selective steam oxidation of $Al_{0.98}Ga_{0.02}As$ to guide the current (to funnel current spreading from annular contact into the central active region), and the optical mode (to confine the optical field in the radial direction) through the central region of the resonator [16]. The diameter of oxide window aperture is 4.5 μm and the diameter of top DBR mirror is 20 μm. To reduce current crowding at the oxide aperture rim, the asymmetric intracavity-contacted VCSELs were fabricated such that the p- and n-contacts are restricted to the opposite sides of the mesa.

4. Small-signal parameters fitting

For standard laser-diode chips, the device capacitance typically dominate the frequency response at the frequencies (10-20 GHz) needed to determine the relevant laser parameters. Additionally, it is not convenient to continually calibrate the measurement equipment to reduce errors; recent results [6] indicate that carrier transport effects seen across the SCH region of a laser diode can give a similar roll-off in frequency response as having a large parasitic capacitance. This effect will also hide the intrinsic dynamic response of the laser.

Whereas a parasitic capacitance can be measured and its effects subtracted from the laser frequency response, the low-pass filter effect of the SCH region cannot. To eliminate all measurement and device parameters that do not vary with bias, the frequency response subtraction technique [17] is used. This leaves the intrinsic response of the laser remaining, which can be curve fitted to provide the relevant parameters (ω_r^2 and γ_r). This technique requires that the parasitic components of the laser diode are not power dependent.

The set-up for modulation response measurements consist of an Anritsu CW generator MG3692A which supplies a frequency swept electrical modulation signal, a coaxial probe for applying the modulation signal directly to the laser chip, ~2 meters of multimode fiber, an Anritsu spectrum analyzer MS2667C, and a high speed Silicon photodiode (25GHz) with a low noise preamplifier. The bare end fiber was actively aligned above the device under test using an x-y-z positioning stage to obtain maximum DC optical power.

The computer sets a DC bias level and then sweeps the RF frequency from 0.1 to 13.1 GHz in 500 MHz steps with constant RF power. At each point, the measured RF power on the spectrum analyzer is recorded, and a separate frequency sweep is taken at different bias levels. For the curve fitting to work well, the first bias point must be fairly close to threshold so that the resonance peak is separate from the peaks in the rest of the sweeps. Once the data is recorded, it can be plotted as in Fig. 2(a), which shows the measured frequency response at different bias levels. This plot illustrates the kind of variation that is common in these measurements; up to several decibels variation can occur from mismatch/reflections, fixture resonances, etc. These variations could be reduced by carrying out time consuming calibrations at regular intervals, but will never be totally removed. Fig. 2(a) shows that variations in the traces are quite large, but are repeatable in the different traces. It is this fact that allows frequency response subtraction to work so well. By subtracting the lower bias trace from the other responses (in dB) [13]

$$S(\omega)=10\lg\left(\frac{\omega_{r1}^4\left(\left(\omega^2-\omega_{r0}^2\right)^2+\omega^2\gamma_{r0}^2\right)}{\left(\left(\omega^2-\omega_{r1}^2\right)^2+\omega^2\gamma_{r1}^2\right)\omega_{r0}^4}\right). \quad (16)$$

All frequency variations that do not change with the laser bias are eliminated from the resulting curves. These curves are shown in Fig. 2(b), where it is obvious that the variations are fully eliminated, leaving a very smooth response. The shape of the response is the intrinsic response of the laser diode at one bias level minus the response at the lower bias level.

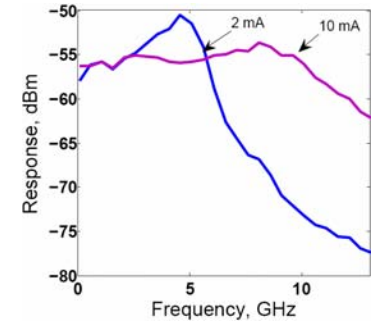

a)

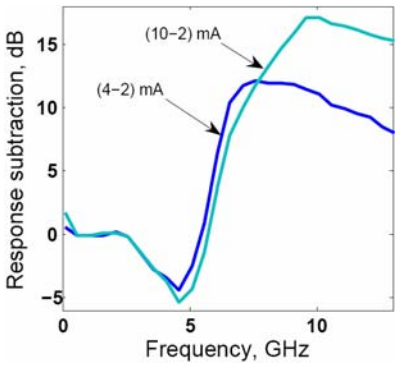

b)

Fig. 2. a) Frequency response measurements on 980 nm MQW VCSEL at different bias levels b) Frequency subtraction traces using data in a) at the stated bias levels.

The measured output power and fitted small-signal modulation parameters (using (16)) for five current points are presented in Table 1.

Table 1. Measured values of VCSEL characterization parameters.

	I_0, mA	I_1, mA			
	2	4	6	8	10
$P_{0,1}$, mW	0.5	1.36	2.12	2.74	3.18
$\gamma_{r0,1}\times10^9$, s^{-1}	4.11	8.26	11.64	13.06	14.01
$\omega^2_{r0,1}$, GHz^2	880	1824	2510	2740	2960

5. Parameter extraction procedure

In order to extract the model parameters, we first relate measured data to our theoretical analysis. We then give some thoughts about the measurement procedure and the preparation of the measured data. Finally, we demonstrate the extraction procedure referring to a data set that was measured and evaluated in Table 1. There are compared the extraction results based on both the simple and the extended rate equation model.

For simplicity, the following analysis is carried out only for the simple rate equation model. However, the same procedure can be applied to the extended model by using the respective equations.

The extended rate equation model contains ten model parameters, which are τ_P, G_d, $N_{W,T}$, τ_{eff}, η_0, η_i, E_p, E_e, E_I and χ. In the following, we relate measured data to these parameters using our above analysis. To clearly distinguish between measured and analytically calculated data new notations are introduced: X, Y and Z are the measured pump current, damping constant and resonance frequency of the small signal response function, respectively. The subscripts 0 and 1 indicate two different operating points. Relating data measured at two operating points to equations (8), (10), and (11), a set of six equations can be formulated [18]:

$$\begin{aligned} \mathrm{X}_{0,1} &= I_{0,1}(N_{P0,1}), \\ \mathrm{Y}_{0,1} &= \gamma_r(N_{P0,1}, N_{W0,1}), \\ \mathrm{Z}_{0,1} &= \omega_r^2(N_{P0,1}, N_{W0,1}) \end{aligned} \tag{13}$$

Equation (11) describes the measured data as a function of the rate equation parameters, the static carrier, and photon numbers. To reduce complexity, the operating – point - dependent photon and carrier numbers $N_{P0,1}$, $N_{W0,1}$ are eliminated in the above equation set using (4) and (5). The number of unknown parameters (our five rate equation parameters) in the resulting nonlinear equation set is the same as the number of equations it consists of. Therefore the equation sets fulfil the necessary condition for solvability, and may be solved numerically using a Levenberg - Marquardt method for the non-linear least-squares [19].

The parameter values may be extracted for the same device from different sets of measured data by varying the operating point far above threshold for the response function. Since the parameters are supposed to be independent of the operating point, at least above threshold their extracted values must also be independent of the bias current of the response function used for the evaluation. Conversely, a dependence on the bias current indicates, that the rate equation model doesn't fit the device under test.

For reliable results, the Levenberg-Marquardt algorithm requires starting values that are not too far from the final solution, thereby avoiding the case when the result may represent only a local minimum instead of the global minimum. To this end, appropriate parameter estimations are easily obtainable, and the measured data set as is shown in the following.

Neglecting E_p, E_e, E_I and setting χ and η_i as unit, the following linear relations between the measured data are calculated from (4), (8), (11) and (12)

$$I_0\left(P_0\right)=\frac{e}{\eta_0 E_g}P_0+\frac{e}{\tau_{eff}}\left(\frac{1}{G_d\tau_P}+N_{W,T}\right), \quad (17)$$

$$\gamma_r\left(\omega_r^2\right)=\tau_P\omega_r^2+\frac{1}{\tau_{eff}}, \quad (18)$$

$$\omega_r^2\left(P_0\right)=\frac{G_d}{\eta_0 E_g}P_0, \quad (19)$$

$$\gamma_r\left(P_0\right)=\frac{\tau_P G_d}{\eta_0 E_g}P_0+\frac{1}{\tau_{eff}}. \quad (20)$$

Straight-line fits to the functions (17) - (20) yield parameter estimates from slopes and axis intersection points. Next, the parameters sets are compared with measurement data for all five points using sum of squares equation:

$$R_y=\sum_{i=1}^{5}\left(\frac{y_m-y_c}{y_m}\right)^2 \quad \text{y=I, } \gamma_r \text{, } \omega_r^2 \quad (21)$$

Here R_I, R_{γ_r} and $R_{\omega_r^2}$ are sum of squares for current-light, damping-light and resonance frequency-light characteristics and presented in Table 2.

Table 2. Different sets of starting values calculated with eq. (17) - (20) and with the data from Table 1.

Parameters	2-4 mA	2-6 mA	2-8 mA	2-10 mA	Average
τ_p, ps	4.31	4.48	4.61	4.62	3.68
$G_d\times10^4$	9.13	8.04	6.11	5.05	8.2
$N_{W,T}\times10^7$	0.022	0.01	0.088	0.066	0.01
τ_{eff}, ns	0.51	0.43	0.63	1.087	0.53
η_0	0.337	0.335	0.301	0.268	0.35
R_I	0.04	0.034	0.019	0.049	0.019
R_{γ_r}	0.214	0.138	0.28	0.247	0.21
$R_{\omega_r^2}$	0.38	0.23	0.467	0.365	0.22

The set of parameters with minimal sum values is chosen as initial value for extended model parameter extraction procedure and presented in the last column in Table 2. The same procedure is repeated step-by-step, with adding one parameter at each time.

The full results of the step-by-step parameter extraction procedure with 5 to 10 parameter schemes, and sum of squares for each characteristic are presented in Table 3.

Table 3. Extraction results averaged with respect to the bias current for different models.

Parameters	6-parameter model	7-parameter model	8-parameter model	9-parameter model	10-parameter model
τ_p, ps	3.68	4.04	3.92	3.94	4.04
$G_d\times10^4$	10.18	17.46	26.15	26.827	28.745
$N_{W,T}\times10^7$	0.01035	0.339	0.557	0.581	0.616
τ_{eff}, ns	0.5279	1.83	1.735	1.727	1.742
η_0	0.881	0.82	0.815	0.852	0.878
η_i	0.776	0.7	0.81	0.864	0.852
$E_p\times10^{-5}$	-	0.87	0.471	0.626	0.593
$E_e\times10^{-7}$	-	-	0.821	0.6711	0.588
E_I, 1/A	-	-	-	16.9	25
χ	-	-	-	-	1.125
R_I	0.027	0.029	0.027	0.014	0.0052
R_{γ_r}	0.02	0.0026	0.017	0.014	0.0051
$R_{\omega_r^2}$	0.18	0.016	0.0173	0.012	0.0043

Table 3 illustrates the situation when at increasing the number of parameters, some parameters are changed weakly (τ_p and η_0), and other parameters (G_d, $N_{W,T}$, τ_{eff}) have larger variation from model to model. The differential quantum efficiency η_0 is related to the slope efficiency of current-light characteristic (first term on the right side of (14)), and also connected with photon lifetime τ_p (see (4)). Because the current-light characteristic has quite linear behavior, such parameters do not change a lot. The parameters G_d and $N_{W,T}$ have the largest difference, especially after including of nonlinear parameters E_p and E_e.

In Fig. 3, the dependence of the carrier number for modal gain (optical gain is calculated using the integral optical gain based on $4\times4\vec{k}\cdot\vec{\mathbf{p}}$ band structure computations for the strained quantum wells [20]) and comparison with linear and nonlinear gain models are presented. The figure illustrates that at the working point, parameters G_d and $N_{W,T}$ for the linear model should be lower than those for nonlinear gain.

Fig. 4 shows the comparison of the experimental results with extracted parameters for 5 and 10 parameter models for all measured characteristics. It can be seen that the 10-parameter model perfectly describes the static and dynamic behavior of VCSEL in the linear and weakly nonlinear regimes.

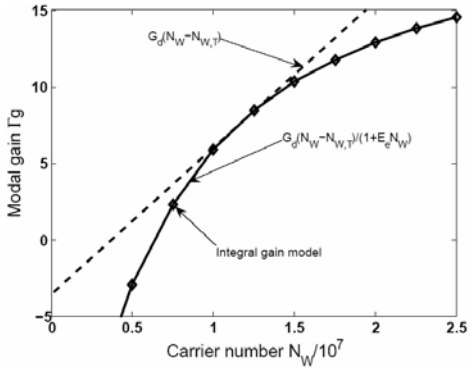

Fig. 3. Dependence of carrier number on modal gain and comparison between different types of gain models.

A strong nonlinear regime (when characteristics decrease with an increase in current (power)) does not have any practical interest, but can be described by more complex theoretical models, ones which cannot be solved analytically.

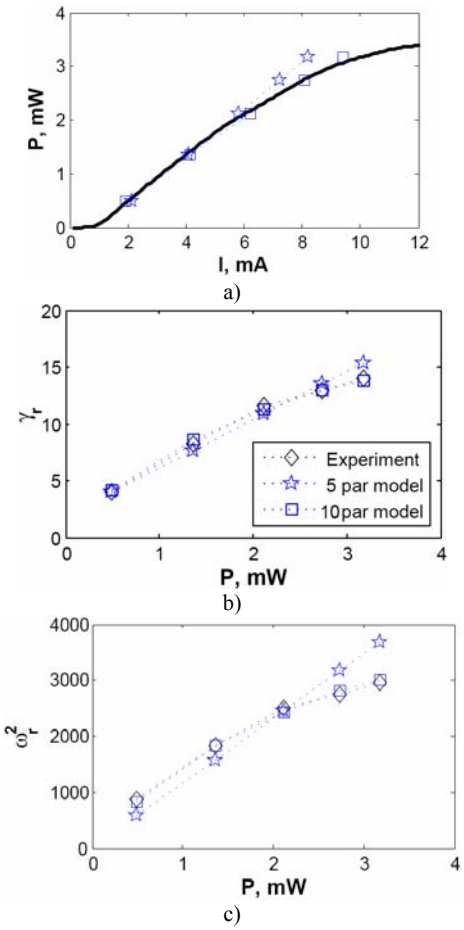

Fig. 4. Comparison of experimental results with extracted parameters for 5 and 10 parameter models for a) light-cur- rent characteristic; b) damping factor versus output power; c) square resonance angular frequency versus output power.

Capture time can be extracted from the modulation characteristics using calculated above parameters. Fig. 5 shows the comparison of measured modulation characteristics with calculated results (from (10)) for different capture times of 0 ps (dashed lines) and 40 ps (solid lines), respectively.

Using the extracted value of transport factor χ (from (13)), the escape time can be calculated, and was found to equal 320 ps.

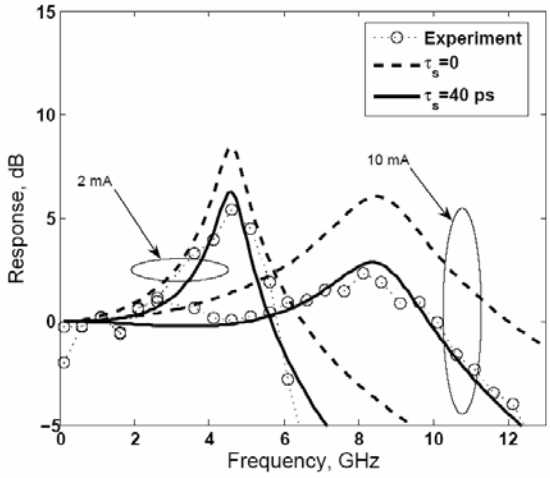

Fig. 5. Relative response measurements for two bias levels and comparison with theoretical results from eq. (10) for different values of capture times. The best agreement at τ_s =40 ps.

6. Conclusions

For the rate equation models of different complexity, we have presented an analysis that relates model parameters to simple DC and small signal measurement data of 980 nm ICOC VCSEL. The parameter extraction model consists of maximum parameters, which can that be analytically described. The calculated parameters where found to have physically reasonable values and exhibit good agreement with measured data in the linear and weakly non-linear regimes.

References

[1] A. V. Krishnamoorthy, L. M. F. Chirovsky, W. S. Hobson, J. Lopata, J. Shah, R. Rozier, J. E. Cunningham, L. A. D'Asaro, IEEE Photon. Technol. Lett. **12**, 609 (2000).

[2] B. J. Thibeault, K. Bertilsson, E. R. Hegblom, E. Strzelecka, P. D. Floyd, R. Naone, L. A. Coldren, IEEE Photon. Technol. Lett. **9**, 11 (1997).

[3] S. Weisser, I. Esquivias, P. J. Tasker, J. D. Ralston, J. Rosenzweig, IEEE Photon. Technol. Lett. **6**, 782 (1994).

[4] J. D. Ralston, S. Weisser, I. Esquivias, E. C. Larkins, J. Rosenzweig, P. J. Tasker, J. Fleissner

IEEE J. Quantum Electron. **29**, 1648 (1993).
[5] I. M. P. Aarts, E. H. Sargent, IEEE J. Quantum Electron. **36**, 469 (2000).
[6] R. Nagarajan, M. Ishikawa, T. Fukushima, R. S. Gills, J. E. Bowers, IEEE J. Quantum Electron. **28**, 1990 (1992).
[7] V. V. Lysak, K. S. Chang, Y. T. Lee, J. Optoelectron. Adv. Mater. **8**(1), 355 (2006).
[8] V. V. Lysak, Y. T. Lee, J. Optoelectron. Adv. Mater. **8**(4), 1601 (2006).
[9] L. V. T. Nguyen, A. J. Lowery, P. C. R. Gurney, D. Novak, IEEE J. Select. Topics Quantum Electron. **1**,494 (1995).
[10] C. Harder, J. Katz, S. Margalit, J. Shacham, A. Yariv, IEEE J. Quantum Electron. **18**, 333 (1982).
[11] R. S. Tucker, I. P. Kaminow, J. Lightwave Technol. **2**, 385 (1984).
[12] L. Bjerkan, A. Røyset, L. Hafskjær, D. Myhre, J. Lightwave Technol. **14**, 839 (1996).
[13] J. C. Cartledge, R. C. Srinivasan, J. Lightwave Technol. **15**, 852 (1997).
[14] K. Petermann, Laser Diode Modulation and Noise. New York: Kluwer Academic, 1988, ch. 2
[15] J. W. Scott, R. S. Geels, S. W. Corzine, L. A. Coldren, IEEE J. Quantum Electron. **29**, 1295 (1993).
[16] G. M. Yang, M. H. MacDougal, P. D. Dapkus, Electron. Lett. **31**, 886 (1995).
[17] P. A. Morton, T. TanbunEk, R. A. Logan, A. M. Sergent, P. F. Sciortino, Jr., D. L. Coblentz IEEE Photon. Technol. Lett. **4**, 133 (1992).
[18] M. Krieg, V. V. Lysak, W. Freude, Radiotekhnika **109**, 14 (1999).
[19] P. E. Gill, W. Murray, SIAM J. Numer. Anal. **1**(5), 977 (1978).
[20] V. V. Lysak, H. Kawaguchi, I. A. Sukhoivanov, Proc. IEE Optoelectron. **152**, 131 (2005).

*Corresponding author: YTLee@gist.ac.kr